UV Diagnostics of Outflow Mechanisms in Five Radio-Quiet Obscured Quasars at Low Redshift

Elise Kesler,[1] Sean D. Johnson,[1] Jonathan Stern,[2] and Zhuoqi Liu[1]

[1] Department of Astronomy, The University of Michigan, 500 S State St, Ann Arbor, MI, 48109, USA
[2] School of Physics and Astronomy, Tel Aviv University, 69978 Tel Aviv, Israel

ABSTRACT

Feedback from active galactic nuclei (AGN) is widely acknowledged as a primary process regulating the growth of massive galaxies, though the mechanisms driving this feedback are debated. Prevailing theories suggest that radio-quiet AGN feedback is driven by radiation pressure acting directly on the interstellar medium (ISM) via dust or by hot winds entraining the ISM, but the relative importance of these mechanisms is uncertain. Ratios of highly ionized UV emission lines serve as effective diagnostics of AGN feedback mechanisms due to their sensitivity to the density structure within ionized clouds. This study presents the first analysis of far-ultraviolet (FUV) spectra from five low-redshift galactic-scale outflows in obscured quasars using Hubble's Cosmic Origins Spectrograph (COS). By comparing narrow-line region UV emission line ratios to theoretical models with varying importance of the two driving mechanisms, we find four out of five targets fall within the radiation pressure-dominated regime. The lowest luminosity object in our sample may have a dynamically important hot wind component, but non-detections prevent a clear conclusion in this case.

1. INTRODUCTION

By incorporating feedback from active galactic nuclei (AGN) as the primary regulator of massive galaxy evolution, many current large-scale cosmological models successfully reproduce key observable phenomena (see Bessiere et al. 2024, and references therein). These include the well-established correlations between the properties of supermassive black holes (SMBH) and their host galaxies (Cattaneo et al. 2009; Kormendy & Ho 2013), the suppression of star formation in massive galaxy halos (Behroozi et al. 2013; Su et al. 2021), and the exponential break in the galaxy luminosity function (Bower et al. 2006; Weigel et al. 2017).

The effectiveness of these models has positioned AGN feedback as a cornerstone of modern theories of massive galaxy evolution (for reviews, see Harrison 2017; Morganti 2017; Martín-Navarro et al. 2018; Laha et al. 2021). However, the mechanisms driving these outflows remain enigmatic, especially for radio-quiet quasars that dominate AGN demographics, but which lack the dramatic radio jets that are observed driving feedback in rarer radio-loud systems (e.g. Hardcastle & Croston 2020).

Two primary theories propose that outflows from radio-quiet quasars result from: (1) direct radiation pressure on dust in the interstellar medium (ISM) or (2) ISM entrainment by a hot wind originating from the nucleus. Determining which of these is the primary driver is a subject of active research and debate (for a review, see Singha et al. 2023).

In the case of radiation pressure-driven winds, absorption and scattering of photons within the large columns of dusty gas surrounding an AGN creates pressure, expelling surrounding material as an outflow (Murray et al. 2005; Ishibashi et al. 2018; Arakawa et al. 2022). The radiation pressure compresses the outflowing gas into a stratified pressure gradient, creating a layered ionization structure with the most highly ionized species in the outermost layers closest to the AGN and lower ionization states in the interior of the clouds (Baskin et al. 2013, 2014; Stern et al. 2014). For radiation pressure-mediated AGN feedback to have a significant influence on galaxy evolution, many models include momentum boosting from multiple scatterings of UV photons by dust grains in ISM clouds (Ishibashi et al. 2018).

In hot wind-driven AGN outflow models, quasi-relativistic winds from the central supermassive black hole (SMBH) collide with the surrounding ISM and produce shocks that propagate in both directions on impact. These shocks produce a hot, volume-filling wind that

can contribute to observed outflows by entraining and accelerating the cooler ISM (King et al. (2011); Faucher-Giguère & Quataert (2012)). With the addition of a surrounding hot wind, cool, outflowing gas clouds are expected to have high density at the cloud/wind in order to maintain equilibrium. The higher gas density created by these winds lowers the ionization parameter, U, and leads to a narrower range of ionization species and lower overall ionization state compared to outflows primarily driven by radiation pressure (Allen et al. 2008; Stern et al. 2016).

Recent surveys have largely characterized AGN outflows by tracing strong optical emission lines from low- and intermediate-ionization species, particularly [O III] (e.g., Greene et al. 2011; Harrison et al. 2014; Sun et al. 2017; Leung et al. 2019; Meena et al. 2021). While strong optical lines serve as sensitive tracers for identifying candidate AGN outflows, alone, they cannot effectively diagnose the mechanisms driving these outflows, as they lack sensitivity to the wide range of ionization states needed to distinguish between hot wind-driven and radiation pressure-driven outflows. As Stern et al. (2016) suggests, emission from highly ionized species offers more precise constraints on the contribution of hot winds in driving outflows.

Emission from highly ionized species is particularly useful because it is sensitive to differing density and pressure conditions of the gas (Stern et al. 2016). Taking the ratios between these lines can constrain the dominant mechanism driving an outflow by comparing measured emission ratios of ionization-sensitive species to the theoretical line ratios expected from models that vary the relative importance of pressure from a hot wind versus radiation pressure. In radiation pressure-dominated outflows, the depth-dependent gas pressure and density produces emission lines across a broad range of ionization states (Dopita et al. 2002; Baskin et al. 2013, 2014; Stern et al. 2014). Conversely, in hot gas-driven outflows characterized by comparatively constant internal density, the ionization range is reduced, confining the emission to a narrower range of ionization states. Thus, constraining the importance of hot wind components relative to radiation pressure necessitates observation of a wide range of highly ionized species. UV emission lines such as O VI, N V, and C IV meet the criteria and are observable with sufficient sensitivity with *HST* COS, making ratios between them particularly well-suited as diagnostic tools.

In a pilot study aiming to constrain AGN feedback mechanisms with UV line emission, Somalwar et al. (2020) obtained the first spatially resolved UV spectra of a prototypical low-z obscured quasar, J1356+1026.

Their *HST* COS G140L spectra revealed O VI/N V line ratios consistent with models of AGN photoionized clouds driven primarily by radiation pressure, ruling out the presence of a dynamically important hot wind in the case of this quasar.

Building on the pilot study (Somalwar et al. 2020), we present the first analysis of a sample of five radio-quiet, low-redshift (z) obscured quasars exhibiting galactic-scale outflows. In order to use nuclear UV emission lines as diagnostics, we obtained *HST* COS observations in the FUV range of the circum-nuclear narrow-line region for all five of our targets. In Section 2, we discuss the target selection process, optical SDSS data, and FUV *HST* COS observations. Our resulting UV and optical emission line fluxes are discussed in Section 3.

To determine if a hot wind component or radiation pressure holds more dynamic importance within these outflows, we compare UV emission line ratios for each to theoretical ratios of hot gas pressure to radiation pressure, $P_{\rm hot}/P_{\rm rad}$, using models from Stern et al. (2016). We discuss these emission line ratios and their implications in Sections 3 and 4.

Throughout our analysis, we adopt a flat Λ cosmological model with values of $H_0 = 70$ km/s/Mpc, $\Omega_m = 0.3$, $\Omega_\Lambda = 0.7$.

2. OBSERVATIONS AND DATA REDUCTION

2.1. *Target Selection*

To gain insights into the relative importance of radiation pressure and hot winds for driving AGN feedback (see discussion in Section 1), we targeted a sample of five radio-quiet obscured quasars exhibiting galactic-scale outflows for COS observations of the O VI, N V, and C IV narrow-line region nuclear emission lines. These highly ionized lines serve as effective diagnostics of AGN feedback mechanisms due to their sensitivity to the density structure within ionized clouds (Stern et al. 2016) .

Radio-quiet obscured quasars are ideal targets for our diagnostics. Dust in the obscured quasar hosts acts as a natural coronagraph, blocking the bright central nucleus and allowing observations of any extended outflows and conditions in the narrow-line region. We targeted high luminosity systems because these are more likely to host outflows, making them excellent laboratories for studying AGN feedback (Zakamska & Greene 2014; Polednikova, J. et al. 2015).

Observing the O VI, N V, and C IV features within the COS FUV window requires redshifts between ≈ 0.1 and ≈ 0.17. Therefore, we identified obscured quasars in this redshift range with evidence for galactic-scale, extended (≈ 10 kpc) outflows previously published in the litera-

ture by Greene et al. (2011), Harrison et al. (2014), and Sun et al. (2017). All three of these surveys identified candidate extended outflows from previous catalogs of Type 2 quasars (Reyes et al. 2008; Mullaney et al. 2013) from the Sloan Digital Sky Survey (SDSS; York et al. 2000) using optical [O III] emission lines as an outflow tracer and observed them with either long-slit or integral field optical spectroscopy. All of our targets are potential or confirmed mergers, which is further discussed in Section 4.

First, we include *J1356+1026*, at $z = 0.123$, which was the subject of a pilot study by Somalwar et al. (2020). It was chosen from Greene et al. (2011) based on their long-slit observations made using the Low-Dispersion Survey Spectrograph 3 (LDSS3, Allington-Smith et al. (1994)) at the Magellan/Clay telescope at the Las Campanas Observatory in Chile. J1356+1026 has the most pronounced extended and kinematically disturbed outflow out of their sample of 15 luminous, obscured, low-z quasars, and they estimate its [O III] emission radius as ≈ 10 kpc (also see Green et al. 2012).

We selected two more targets from (Greene et al. (2011)): J1222−0007 and J0841+0101. *J1222−0007*, at $z=0.173$, is a spiral galaxy with an [O III] emission radius of ≈ 12.6 kpc and relatively high emission-line width (>500 km s^{-1}) (Greene et al. 2011). *J0841+0101*, at $z=0.111$, has a reported [O III] emission radius of ≈ 10 kpc (Greene et al. 2011).

We targeted *J1000+1242*, at $z=0.148$, based on the GMOS South IFU observations from Harrison et al. (2014). They selected it from the parent catalog of Mullaney et al. (2013) as part of a representative study of type 2, low-z obscured quasars. They report an extended [O III] emission-line region radius of 4.3 ± 1.8 kpc.

We targeted *J1255−0339*, at $z=0.169$, based on the Magellan long-slit observations in Sun et al. (2017). It had the most extended narrow-line region in their sample of 12 nearby luminous obscured AGN, with a $R_{\rm NLR}$ (narrow-line region radius) of 33.5 ± 1.4 kpc.

2.2. *SDSS Optical Data*

To ensure a uniform analysis of the sample drawn from a number of AGN catalogs and produce the BPT diagram discussed in Section 3, we performed our own emission line flux measurements of the nuclear optical spectra for the five targets from the SDSS DR17 Data Release (Abdurro'uf et al. 2022). We measured emission in [N II], Hα, [O III], and Hβ. Prior to taking flux measurements, we subtracted a linear continuum around the emission lines, fit to nearby line-free spectral regions.

Table 1: Summary of *HST* COS observations.

Object	Grating	$t_{\rm exp}$ [s]	Start Date	Observation ID
J1356+1026	G140L	5200	2019-06-12	ldhv01010
J0841+0101	G140L	480	2020-02-26	le3i03010
J1000+1242	G140L	700	2020-05-26	le3i04010
J1222−0007	G140L	500	2020-05-18	le3i07010
	G130M	500	2020-05-18	le3i07010
J1255−0339	G130M	2300	2020-07-04	le3i08010
	G140L	2400	2020-07-04	le3i08020

We performed the continuum fit and subtraction separately for the Hα+[N II] and Hβ+[O III] regions.

Due to line blending in the Hα+[N II] region, we measured optical fluxes by fitting Gaussian profiles to each emission line. In most cases, the emission lines were blended or poorly described by a single Gaussian, so we used multiple Gaussian fitting models. We modeled both doublets ([N II] $\lambda\lambda 6550, 6585$ Å and [O III] $\lambda\lambda 4960,$ 5008 Å) as double-peaked Gaussians with a fixed amplitude ratio of 2.95, the expectation given by the theory of atomic transitions Osterbrock & Ferland (2006).

Within the Hα+[N II] region, we used three Gaussian components — one broad and two narrow — to fit all of the spectra except J0841+0101, which required only two components (one broad and one narrow). Since line width is expected to be consistent between the Hα and [N II] emission lines of obscured quasars, we fixed each component to share values (ie., the broad Hα and broad [N II] Gaussian components had the same line width).

Within the Hβ+[O III] region, one broad and one narrow Gaussian effectively modeled the emission lines for J1000+1242, J0841+0101, and J1356+1026. An additional narrow component was needed for J1222−0007. In the case of J1255−0339, an additional narrow component was necessary to model the [O III] $\lambda\lambda 4960,$ 5008 Å doublet, but adding a corresponding Hβ component did not improve the fit. Thus, we modelled it with three Gaussians fitting [O III] and two fitting Hβ. Again, similar components shared widths (ie., we modelled broad Hβ and broad [O III] with the same line width).

We applied a χ^2 minimization routine with the `lmfit` module (Newville et al. 2015) to find the best-fit model parameters for each region. Due to degeneracies between the line fluxes, widths, and redshifts of the the multi-Gaussian profiles, we evaluated the total flux posteriors using Markov Chain Monte Carlo (MCMC) methods from the `emcee` module (Foreman-Mackey et al. 2013) with walker start positions set around the best fit from the χ^2 minimization routine. The values and uncertain-
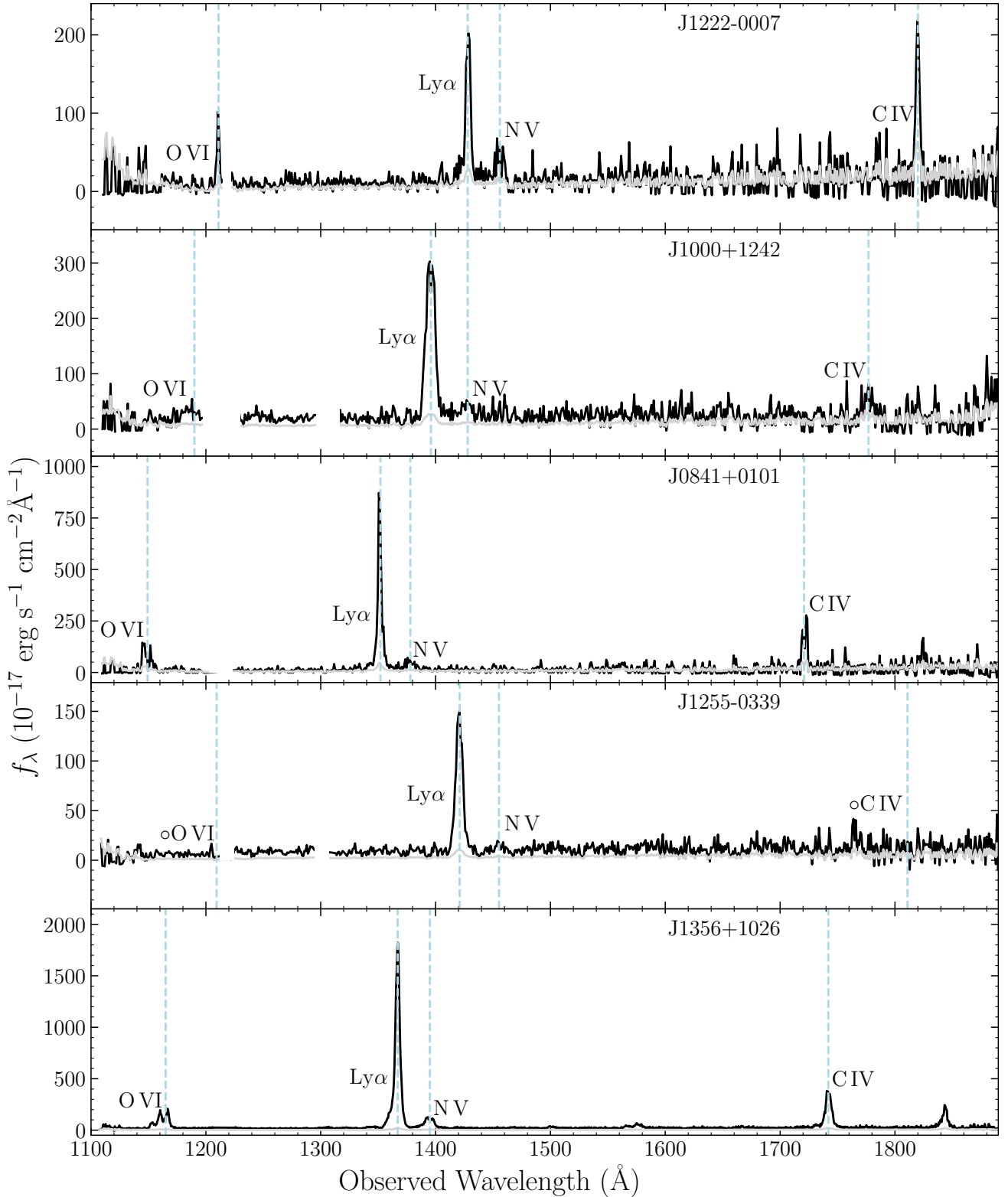
Figure 1: COS UV nuclear spectra for all five of our targets. Dashed light blue lines mark the expected location of the labeled spectral line given the target's redshift. In the case of observed doublets (O VI $\lambda\lambda$1031, 1037Å, N V $\lambda\lambda$1238, 1242 Å, and C IV $\lambda\lambda$1548, 1550 Å) the blue line is located at the midpoint of the expected location of each emission line. The two reported non-detections, O VI and C IV for J1255-0339, are denoted on their respective labels with open circles. To aid the visual inspection of emission lines, we have masked out the Lyα and O I geocoronal lines, where applicable, and set the y-axis limits so Lyα is similarly scaled for all five.

ties reported in Table 2 are based on the posterior for each total line flux marginalized over other model parameters.

2.3. *HST COS Observations and Data Reduction*

To cover the wavelength range needed for our diagnostics, we obtained far-ultraviolet (FUV) nuclear spectra for our five targets from the Cosmic Origins Spectrograph (COS) on the *Hubble Space Telescope* (*HST*). The COS observations of J1356+1026 are from a pilot program (Somalwar et al. 2020, PID 15280). COS observations of the other four obscured quasars came from a new proposal (PID 15935). All observations used for this analysis are summarized in Table 1.

The new *HST* COS observations were taken primarily with the G140L grating, but also supplemented with G130M in some cases. G140L has a relatively low resolution (resolving power ranging from 1,500-4,000) and was chosen for its wide wavelength range. Our G140L spectra cover wavelengths between ≈1100-1900 Å. We used the higher-resolution G130M (resolving power ranging from 12,000-16,000) for two objects with O VI emission in close proximity to geocoronal Lyman alpha (J1222-0007 and J1255-0339). We spliced the G130M spectra into the G140L spectra in the spectral region near O VI impacted by geocoronal emission for these two objects, as the higher resolution of G130M enables it to better separate O VI emission of the AGN from contaminating geocoronal emission.

We retrieved the 1D spectrum associated with each exposure reduced using the CALCOS pipeline (Version 3.4.3; Kaiser et al. 2008) from the MAST archive. We then combined the individual exposures into final coadded spectra after masking out out pixels with data quality flags. In particular, we included only pixels with no anomalies or flagged only as in the detector shadow. We included pixels with detector shadow flags because the data reduction flat-fielding is sufficient to correct for the detector wire shadow so that any remaining artifacts are undetectable at our observed S/N (Soderblom et al. 2022). Our target spectra were taken with all four FP-POS positions, the default COS fixed-pattern noise offset setting. We co-added spectra onto a rebinned wavelength grid with a pixel scale of 1 Å for visualization purposes for all five of the targets.

In order to correct for the effects of Milky Way dust extinction, we used the extinction curve from Fitzpatrick (1999) implemented in the `Extinction` package (Barbary 2021) and A_V values estimated in the direction of each obscured quasar from the extinction map in Schlafly & Finkbeiner (2011). The resulting coadded and extinction-corrected spectra are shown in Figure 1.

Within these spectra, we observe emission in the O VI $\lambda\lambda$1031, 1037 Å doublet; the N V $\lambda\lambda$1238, 1242 Å doublet; and the C IV $\lambda\lambda$1548, 1550 Å doublet. The process we used to measure these emission line fluxes is described in Section 2.4, and the results are reported in Section 3.

2.4. *UV Flux Measurements*

Since the O VI, N V, and C IV UV emission lines are generally not blended with strong lines from other species, we measured their fluxes by applying direct Simpson integration to each individual emission line after subtracting a linear continuum fitted to nearby line-free spectral regions. We do not treat individual doublet lines separately; i.e. the reported doublet emission flux values are the sum of both lines. During the integration process, we estimated flux errors from Poisson counting statistics. To verify the accuracy of these estimates, we also calculated the mean flux per pixel from surrounding line-free continuum areas for each individual line and determined its standard deviation. The consistency between these methods led us to adopt the Poisson error estimates which are reported here. We adopt a 3σ detection threshold, and report corresponding upper limits in the cases of non-detections.

The close proximity of the $\lambda\lambda$1031, 1037 Å doublet to geocoronal Lyα resulted in partial blending in the cases of J1222−0007 and J1255+0339, despite the use of G130M data. To determine the extent of blending for J1222−0007, we compared the FWHM of the other measured doublets (N V $\lambda\lambda$1238, 1242 Å and C IV $\lambda\lambda$1548, 1550 Å) to the expected doublet separation. We found that the emission blue of geocoronal Lyα at the expected location of O VI had the smallest FWHM despite having the largest expected doublet separation. As a result, we hypothesized that the singular visible O VI emission line blue of geocoronal Lyα was the 1031 emission line, and the 1037 emission line was blended with geocoronal Lyα. To determine if this assumption was viable and further examine the extent of the blending, we fit two Gaussians — one to each emission line in the doublet, with a shared emission line width — to the N V $\lambda\lambda$1238, 1242 Å and C IV $\lambda\lambda$1548, 1550 Å doublets and used the velocity dispersions from those fits as an initial guess in a fit of O VI $\lambda\lambda$1031, 1037 Å, along with an additional Gaussian fit to geocoronal Lyα. Fixing the O VI doublet Gaussian widths to the N V velocity dispersion resulted in a good fit, supporting our hypothesis that the 1037 line was blended with geocoronal Lyα. However, the C IV emission line in this case had a significantly lower

Table 2: UV and optical nuclear emission line fluxes

	Line	Flux	Centroid	SNR
		$(10^{-15}$ erg cm^{-2} s$^{-1})$	(Å)	
J1356+1026	H I Lyα	94 ± 0.4	1365	240.0
	N V 1238.82/1242.80	9.5 ± 0.1	1394	94.5
	O VI 1031.92/1037.61	17 ± 0.2	1162	88.7
	C IV 1548.19/1550.77	26 ± 0.4	1740	58.4
	[O III] 4960/5008	167 ± 0.6		
	Hβ	18 ± 0.2		
	[N II] 6550/6585	27 ± 0.3		
	Hα	63 ± 0.5		
J0841+0101	H I Lyα	34 ± 1.2	1350	29.6
	N V 1238.82/1242.80	3.8 ± 0.4	1378	11.6
	O VI 1031.92/1037.61	8.6 ± 0.9	1149	11.3
	C IV 1548.19/1550.77	11 ± 1.0	1720	7.3
	[O III] 4960/5008	100 ± 0.5		
	Hβ	8.5 ± 0.1		
	[N II] 6550/6585	12 ± 0.1		
	Hα	35 ± 0.2		
J1000+1242	H I Lyα	27 ± 0.9	1396	32.2
	N V 1238.82/1242.80	2.5 ± 0.2	1424	13.4
	O VI 1031.92/1037.61[a]	5.2 ± 0.3	1188	19.5
	C IV 1548.19/1550.77	7.3 ± 0.8	1779	7.7
	[O III] 4960/5008	119 ± 1.5		
	Hβ	9.0 ± 0.1		
	[N II] 6550/6585	32 ± 2.0		
	Hα	51 ± 2.0		
J1222-0007	H I Lyα	10 ± 0.7	1426	15.9
	N V 1238.82/1242.80	3.2 ± 0.4	1455	9.2
	O VI 1031.92/1037.61	4.66 ± 0.94	1213	9.7
	C IV 1548.19/1550.77	8.9 ± 1.4	1817	6.0
	[O III] 4960/5008	109 ± 0.3		
	Hβ	11 ± 0.1		
	[N II] 6550/6585	19 ± 0.2		
	Hα	45 ± 0.3		
J1255-0339	H I Lyα	11 ± 0.3	1421	37.0
	N V 1238.82/1242.80	0.9 ± 0.05	1450	45.0
	O VI 1031.92/1037.61[b]	<0.9	1209	7.5
	C IV 1548.19/1550.77[c]	<3.7	1811	—
	[O III] 4960/5008	10 ± 0.1		
	Hβ	2.4 ± 0.1		
	[N II] 6550/6585	9.7 ± 0.2		
	Hα	14 ± 0.2		

[a] As only the 1031 line is visible for this object, we estimate the reported 1037 flux as being between one and two times the 1031 flux, and add it to the 1031 value. The added estimate is reported here, and the errors reflect the uncertainty in this method, which is further described in Section 2.4)

[b] Upper-limit flux estimated as the three sigma limit from a double Gaussian fit with fixed parameters (detailed more in Section 2.4)

[c] Upper-limit flux estimate based on integrated flux/counts in the surrounding region (detailed more in Section 2.4)

velocity dispersion, and modeling the C IV doublet with two separate Gaussians proved difficult as it was more peaked than expected.

Given these results, we estimated the total O VI flux for J1222−0007 by considering the theoretical expectation for ratios between the O VI 1031 and 1037 emission lines. In the optically thin limit, the 1031 emission line is expected to be approximately twice as strong as the 1037 line, but in the optically thick limit there is an approximately 1:1 ratio (Draine 2011). We are unsure which is the case, particularly since no conclusive ratio emerges upon examining the two spectra we have that show visibly distinct emission lines in the O VI doublet, J1356+1026 and J0841+0101 — the doublet emission lines have about a 1:1 ratio in the J1356+1026 case, but J0841+0101 is closer to a 2:1 ratio. Thus, we estimate the total flux is between the optically thin and optically thick expectations:

$$f_{1031} + 0.5(f_{1031}) \leq f_{1031/1037} \leq 2(f_{1031}) \qquad (1)$$

where $f_{1031/1037}$ is the total O VI doublet flux and f_{1031} is the measured 1031 emission line flux. We have expanded our reported uncertainty to include all values between these possibilities, and our reported flux is their midpoint, $f_{1031/1037} = f_{1031} + 0.75(f_{1031})$.

As O VI was similarly close to geocoronal Lyα for J1255+0339, we performed the same kind of Gaussian analysis. However, the N V doublet was significantly broader than the single visible line blue of geocoronal Lyα in this case, and since C IV is a non-detection for this target, we could not use that for comparison. Thus, we cannot conclude if the visible emission is a true O VI emission line, and we classify it as a non-detection.

Proximity of O VI to geocoronal Lyα also introduced additional uncertainty in the case of J1000+1242. Though a similar FWHM comparison to the one described at the beginning of this section showed the O VI doublet to be distinctive from geocoronal Lyα, it was difficult to define the linear continuum and define the integration boundaries. Due to the generally broad line profiles for J1000+1242, it was difficult to define integration boundaries for the other observed emission lines as well. To account for this added uncertainty, we adjusted the bounds repeatedly across the the range of reasonable limits, and found flux differences of $\pm \approx 10\%$. We include this additional systematic uncertainty in our reported measurements and interpretation in this case.

Our two non-detections, C IV and O VI in the spectrum of J1255+0339, are reported here as upper-limit flux estimates. We estimated an upper-limit flux for C IV by calculating the average flux per count multiplied by the gross counts within 23 Å – the approximate max-

imum width of this object's Lyα emission line – around the expected location of C IV, based on the target's redshift. This method was not useful for estimating the O VI upper-limit flux, since the area surrounding the expected line location included geocoronal Lyα. Thus, we estimated O VI as the three sigma limit from a double Gaussian fit with the redshift fixed to the optical expectation and the velocity dispersion fixed to that of Lyα for the same object.

3. RESULTS

To confirm the AGN nature of our objects and contextualize them within the general AGN population, we produced a BPT diagram (Figure 2, left panel) with diagnostic boundaries from Kewley et al. (2006), separating AGN from star-forming galaxies on a plot of [N II]/H α vs [O II]/H β. The BPT diagram confirms that all five targets fall within the expected range for Type 2 AGN. In the right panel of Figure 2, we plot the [O III] λλ4960, 5007 Å line luminosities versus redshifts for our sample, alongside data from the obscured quasar catalog in Reyes et al. (2008). With the exception of J1255−0339, our targets rank among the more luminous obscured quasars within their redshift range.

The UV spectra exhibit notable variations in line strengths across the sample. To provide context, we qualitatively compare the spectral line profiles of our targets to those of J1356+1026, which was previously examined in Somalwar et al. (2020). The line ratios in J0841+0101 and J1000+1242 closely resemble those of J1356+1026, although J1000+1242 displays noticeably broader spectral features. J1222−0007 exhibits a relatively high C IV to Lyα flux ratio compared to the other targets. J1255−0339, in contrast, shows weak UV emission in general, with non-detections of C IV and O VI; we provide upper-limit flux estimates for these emission lines based on its expected location (see Section 2.4 for details on this estimation).

Table 2 summarizes the optical and UV line fluxes for all five targets, along with counts and signal-to-noise ratios for the UV lines only. Diagnostic ratios between the UV lines are shown and discussed in Section 4.

4. DISCUSSION

In Figures 3 and 4, we compare our measured optical and UV emission line ratios of [O III], O VI, C IV, and N V to the models from Stern et al. (2016). The left panel of Figure 3 is our most substantial diagnostic, as it specifically examines UV line ratios in a plot of log(O VI/N V) vs log(O VI/C IV).

The observed O VI/N V and O VI/C IV line ratios are relatively consistent with radiation pressure-dominated
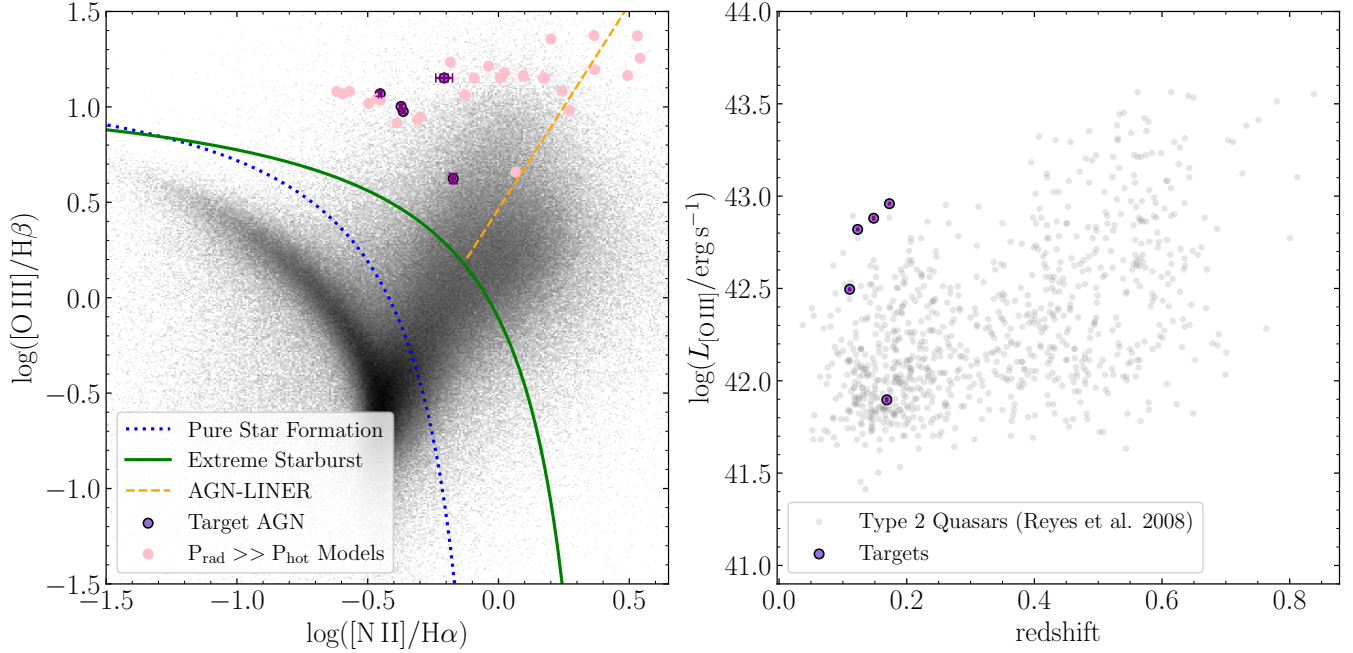
Figure 2: *Left panel:* BPT diagram confirming identification of objects as AGN, with target obscured quasars in purple and SDSS galaxies in greyscale for comparison (Abdurro'uf et al. (2022), Brinchmann et al. (2004), Kauffmann et al. (2003), Salim et al. (2007), Tremonti et al. (2004)). The solid green and dotted blue lines are the extreme starburst and pure star formation classification lines from Kewley et al. (2006). The Seyfert-LINER line from Kauffmann et al. (2003) is in orange. Error estimates for both axes are plotted in light purple. The predictions for the Radiation Pressure Confinement (RPC) model in the $P_{\rm rad} >> P_{\rm hot}$ limit are shown in pink. *Right panel:* [O III] luminosities measured from SDSS spectra vs redshift for our five targets plotted against those of the Type 2 Quasars catalogue presented in Reyes et al. (2008). The 68% confidence interval errors for the [O III] luminosities plotted in light purple are smaller than the data points.

models $(P_{\rm hot} < P_{\rm rad})$ for four out of five of our targets (J1356+1026, J0841+0101, J1222−0007, and J1000+1242) in the $\log(O\ VI/N\ V)$ vs $\log(O\ VI/C\ IV)$ diagnostic plots. These targets are shown in purple in Figure 3. The pilot study (Somalwar et al. 2020) echoed these findings, as it also found the J1356+1026 line ratios fall within the radiation-pressure dominated regime.

In the $\log(O\ VI/[O\ III])$ vs $\log(O\ VI/C\ IV)$ diagnostic plots (right panel of Figure 3), the targets do not fall within the expected model uncertainty. Thus, although they appear to align more with the radiation pressure-dominated regime, a precise conclusion cannot be made.

Concluding what regime the J1255+0339 line ratios fall within is not possible with our results due to the non-detections of C IV and O VI, the upper limit estimates for which are shown as dashed blue lines in Figure 3. The estimates suggest the possibility it falls within the hot gas-pressure dominated regime, but higher sensitivity measurements without geocoronal Lyα contamination are required to diagnose this object. J1255+0339 is the least luminous quasar in our sample, and displayed

the weakest emission in the UV. It is also the highest redshift quasar in our sample, with $z=0.173$.

We include individual line ratios on the right panel of Figure 3 which further exemplify the diagnostics described in the previous paragraphs. The top right panel compares $\log(O\ VI/N\ V)$ to $P_{\rm hot} < P_{\rm rad}$ and the bottom right panel compares $\log(O\ VI/C\ IV)$ to $P_{\rm hot} < P_{\rm rad}$. Though single line ratios are not as effective diagnostically as comparative ones, we include these to demonstrate how closely each object adheres to model predictions for each reported ratio.

Though we obtained high-quality measurements of Lyα for each object, we did not include them in our analysis due to discrepancies between observations and models we believe is due to radiative transfer effects. To quantify this, we compared the Balmer decrement (Hα/Hβ), a reliable estimate of dust extinction (Domínguez et al. 2013), to the ratio between Lyα and Hα, as shown in shown in Figure **??**. All of our targets fell well below the expected Lyα/H$\alpha \approx 8.7$ ratio at recombination from Hayes (2015), which suggests a high degree of scattering affects these measurements. Com-
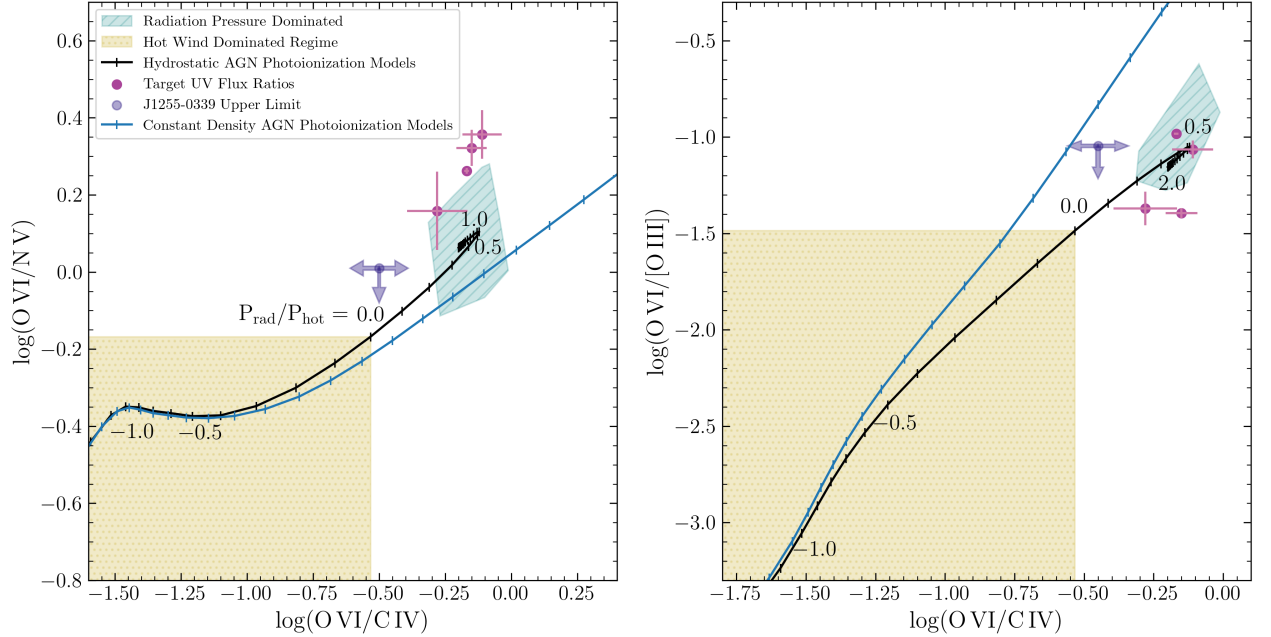
Figure 3: UV diagnostic line ratio diagrams for the archival sample of five obscured quasars with constraints on these transitions. In both panels, the observed line ratios are shown as purple points with error bars, and the upper-limit flux estimates for the O VI and C IV non-detections for J1255−0339 are shown as dashed blue lines with arrows indicating the estimated possible values. Models of AGN photoionized gas varying $P_{\rm hot}/P_{\rm rad}$ from Stern et al. (2016) ($Z/Z_{\rm sun} = 2Z_{\rm sun}$) are shown in solid black, with ticks marking steps of $0.1\,{\rm dex}$ in $P_{\rm hot}/P_{\rm rad}$. We represent the estimated radiation pressure-dominated regime by shading in teal the region covered by $P_{\rm rad} >> P_{\rm hot}$ models with parameters ranging from $1 < Z/Z_{\rm sun} < 4$, $-1.8 < \alpha_{\rm ion} < -1.4$, and $100pc < r < 10kpc$. A rough estimate of the hot wind phase regime is shown in light yellow; this is simply the region where $P_{\rm hot} > P_{\rm rad}$, and not informed by models. For comparison, the ratios for models with constant density are shown in blue. *Left panel*: UV diagnostic line ratio diagram with O VI/N V versus O VI/C IV. The radiation-pressure dominated models accurately predict COS spectra of four of the obscured quasars in this diagnostic regime, indicating they are in the radiation-pressure dominated limit. The results of J1255−0339 are inconclusive due to non-detections, but the upper limit observations suggest it may fall within the hot-gas dominated regime. *Right panel*: UV diagnostic line ratio diagram with O VI/[O III] versus O VI/C IV.Two of the objects roughly fall within the radiation pressure-dominated region, although they fall outside the model uncertainty range. Two more targets are not well-described by the models, and results for J1255−0339 are once again inconclusive due to non-detections.

parison with expectations from the varying $P_{\rm hot}/P_{\rm rad}$ models shows our targets are consistently dustier than the models, and the two dustiest targets are perhaps seen through an external dust screen.

Notably, all five targets are potential mergers. J1222−0007 has a secondary source ≈ 4.7 arcseconds away (Molyneux et al. 2023). J0841+0101's dual AGN classification is tentative, and is discussed in (Foord et al. 2020; Comerford et al. 2015; Pfeifle et al. 2023). Sun et al. (2017) suggests that J1255−0339 may be in late stages of a merger based on its morphology and high infrared luminosity. As noted within their appendix, despite its beautiful $\approx$60 kpc spiral features, thought to be

tidal tails ionized by the central AGN, it has received little attention in the literature. J1356+1026 is made up of two merging nuclei separated by ≈ 2.5 kpc, as shown by its double-peaked [O III] emission (Dutta & Srianand (2022), Ramos Almeida et al. (2022), Molyneux et al. (2023)).

This may support the theory that Type 2 quasars are triggered by gas funneled to the nucleus during galaxy interactions, as discussed in (Pierce et al. 2023).

5. CONCLUSIONS

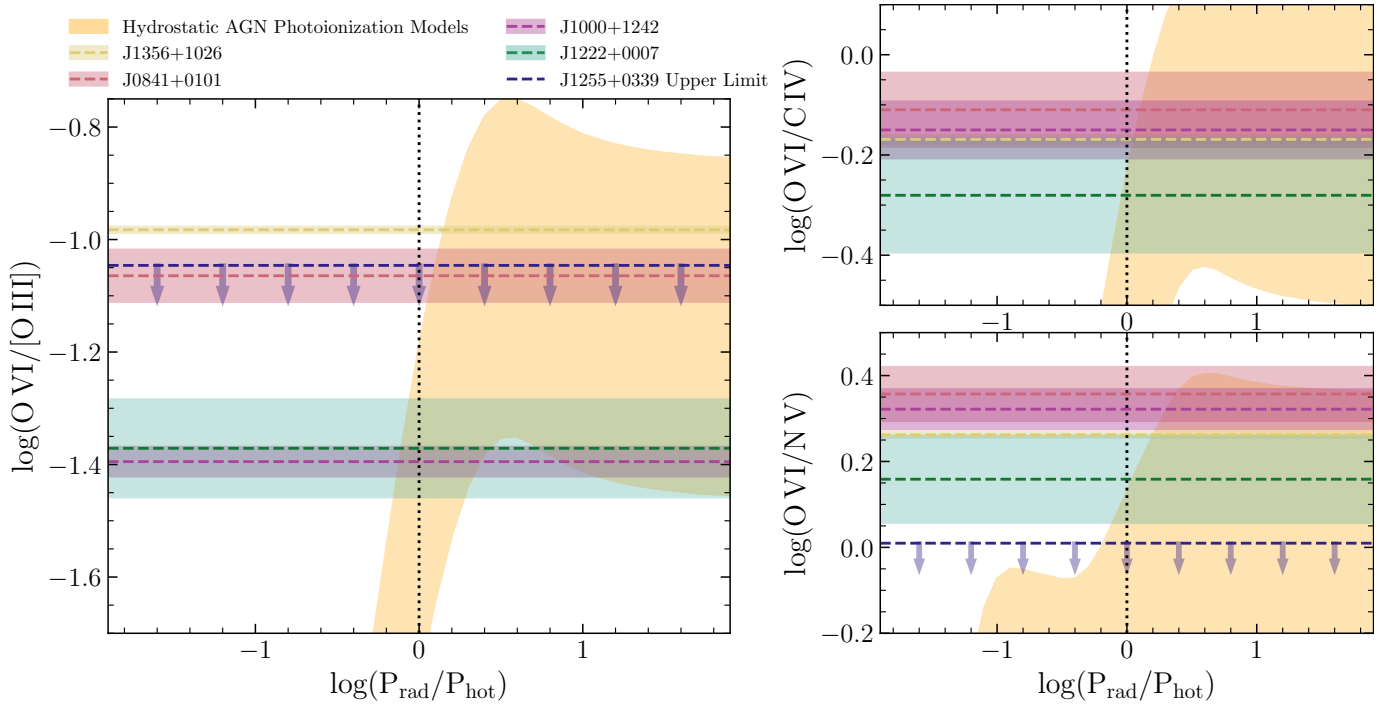This survey examined five radio-quiet, low-z, luminous AGN exhibiting galactic-scale outflows in order to

Figure 4: Predicted line ratios versus the relative importance of radiation pressure and hot gas pressure for the theoretical models from (Stern et al. 2016), shown with the UV diagnostic line ratios for the archival sample of five obscured quasars and their respective 1-σ errors. Each object is plotted with a different color to aid in visual inspection, particularly due to the large O VI/[O III] error associated with J1222−0007 on the bottom left plot. The legend in the upper left panel applies to all three plots. The J1255−0339 upper-limit O VI flux estimates are shown with a dashed blue line, where applicable. As both O VI and C IV are non-detections for this object, we have omitted J1255−0339 from the O VI/C IV ratio plot on the top right. In all three plots, a black dotted vertical line indicates where $P_{hot}/P_{rad} = 0$ in the models. Though single line ratios are not as effective diagnostics as the comparative ones in Figure 3, flux measurements intersecting to the left of this dotted line suggest hot gas domination, while those to the right indicate radiation pressure domination.

diagnose the mechanisms driving AGN feedback. By comparing HST COS observations of narrow-line region nuclear emission lines in the FUV range to estimates of P_{rad}/P_{hot}, the ratio of hot gas pressure to radiation pressure predicted by theoretical models, we constrain which driving mechanism dominates the outflows in each case.

Our UV diagnostics suggest that four of our five targets (J1356+1026, J0841+0101, J1222+0007, and J1000+1242) align with models predicting radiative-pressure dominated outflows, reflecting the results of a pilot study by Somalwar et al. (2020). The remaining target (J1255+0339 may include a dominant or partial hot wind mechanism, but non-detections of O VI and C IV prevent a robust conclusion.

Comparisons of UV and optical emission line ratios are similarly inconclusive, as they do not appear to fall within the expected model uncertainty.

Although this sample is too small to give conclusive evidence on primary drivers of AGN outflows, it suggests that although the diagnosable targets fall within the radiation pressure-dominated regime, we cannot rule out that both theorized mechanisms could play a role in observed AGN feedback. Further investigations in the UV and optical may further constrain the contribution of a hot wind component and provide conclusions for a broader sample of quasars.

REFERENCES

Abdurro'uf, Accetta, K., Aerts, C., et al. 2022, The Astrophysical Journal Supplement Series, 259, 35, doi: 10.3847/1538-4365/ac4414

Allen, M. G., Groves, B. A., Dopita, M. A., Sutherland, R. S., & Kewley, L. J. 2008, The Astrophysical Journal Supplement Series, 178, 20, doi: 10.1086/589652

Allington-Smith, J., Breare, M., Ellis, R., et al. 1994, Publications of the Astronomical Society of the Pacific, 106, 983, doi: 10.1086/133471

Arakawa, N., Fabian, A. C., Ferland, G. J., & Ishibashi, W. 2022, Monthly Notices of the Royal Astronomical Society, 517, 5069, doi: 10.1093/mnras/stac3044

Barbary, K. 2021, extinction: Dust extinction laws, Astrophysics Source Code Library, record ascl:2102.026

Baskin, A., Laor, A., & Stern, J. 2013, Monthly Notices of the Royal Astronomical Society, 438, 604, doi: 10.1093/mnras/stt2230

—. 2014, Monthly Notices of the Royal Astronomical Society, 445, 3025, doi: 10.1093/mnras/stu1732

Behroozi, P. S., Wechsler, R. H., & Conroy, C. 2013, ApJ, 770, 57, doi: 10.1088/0004-637X/770/1/57

Bessiere, P. S., Almeida, C. R., Holden, L. R., Tadhunter, C. N., & Canalizo, G. 2024, QSOFEED: The relationship between star formation and AGN Feedback. https://arxiv.org/abs/2405.06421

Bower, R. G., Benson, A. J., Malbon, R., et al. 2006, MNRAS, 370, 645, doi: 10.1111/j.1365-2966.2006.10519.x

Brinchmann, J., Charlot, S., White, S. D. M., et al. 2004, MNRAS, 351, 1151, doi: 10.1111/j.1365-2966.2004.07881.x

Cattaneo, A., Faber, S. M., Binney, J., et al. 2009, Nature, 460, 213, doi: 10.1038/nature08135

Comerford, J. M., Pooley, D., Barrows, R. S., et al. 2015, Merger-driven Fueling of Active Galactic Nuclei: Six Dual and Offset Active Galactic Nuclei Discovered with Chandra and Hubble Space Telescope Observations. https://arxiv.org/abs/1504.01391

Domínguez, A., Siana, B., Henry, A. L., et al. 2013, The Astrophysical Journal, 763, 145, doi: 10.1088/0004-637x/763/2/145

Dopita, M. A., Groves, B. A., Sutherland, R. S., Binette, L., & Cecil, G. 2002, The Astrophysical Journal, 572, 753, doi: 10.1086/340429

Draine, B. T. 2011, Physics of the Interstellar and Intergalactic Medium

Dutta, R., & Srianand, R. 2022, Monthly Notices of the Royal Astronomical Society, 516, 4338–4345, doi: 10.1093/mnras/stac2483

Faucher-Giguère, C.-A., & Quataert, E. 2012, Monthly Notices of the Royal Astronomical Society, 425, 605–622, doi: 10.1111/j.1365-2966.2012.21512.x

Fitzpatrick, E. L. 1999, PASP, 111, 63, doi: 10.1086/316293

Foord, A., Gültekin, K., Nevin, R., et al. 2020, The Astrophysical Journal, 892, 29, doi: 10.3847/1538-4357/ab72fa

Foreman-Mackey, D., Hogg, D. W., Lang, D., & Goodman, J. 2013, PASP, 125, 306, doi: 10.1086/670067

Green, J. C., Froning, C. S., Osterman, S., et al. 2012, ApJ, 744, 60, doi: 10.1088/0004-637X/744/1/60

Greene, J. E., Zakamska, N. L., Ho, L. C., & Barth, A. J. 2011, ApJ, 732, 9, doi: 10.1088/0004-637X/732/1/9

Hardcastle, M., & Croston, J. 2020, New Astronomy Reviews, 88, 101539, doi: https://doi.org/10.1016/j.newar.2020.101539

Harrison, C. M. 2017, Nature Astronomy, 1, 0165, doi: 10.1038/s41550-017-0165

Harrison, C. M., Alexander, D. M., Mullaney, J. R., & Swinbank, A. M. 2014, MNRAS, 441, 3306, doi: 10.1093/mnras/stu515

Hayes, M. 2015, Publications of the Astronomical Society of Australia, 32, doi: 10.1017/pasa.2015.25

Ishibashi, W., Fabian, A. C., & Maiolino, R. 2018, Monthly Notices of the Royal Astronomical Society, doi: 10.1093/mnras/sty236

Kaiser, M. E., Hodge, P. E., Keyes, C., et al. 2008, in Society of Photo-Optical Instrumentation Engineers (SPIE) Conference Series, Vol. 7014, Ground-based and Airborne Instrumentation for Astronomy II, ed. I. S. McLean & M. M. Casali, 70146G, doi: 10.1117/12.790239

Kauffmann, G., Heckman, T. M., Tremonti, C., et al. 2003, Monthly Notices of the Royal Astronomical Society, 346, 1055–1077, doi: 10.1111/j.1365-2966.2003.07154.x

Kewley, L. J., Groves, B., Kauffmann, G., & Heckman, T. 2006, MNRAS, 372, 961, doi: 10.1111/j.1365-2966.2006.10859.x

King, A. R., Zubovas, K., & Power, C. 2011, Monthly Notices of the Royal Astronomical Society: Letters, 415, L6–L10, doi: 10.1111/j.1745-3933.2011.01067.x

Kormendy, J., & Ho, L. C. 2013, ARA&A, 51, 511, doi: 10.1146/annurev-astro-082708-101811

Laha, S., Reynolds, C. S., Reeves, J., et al. 2021, Nature Astronomy, 5, 13, doi: 10.1038/s41550-020-01255-2

Leung, G. C. K., Coil, A. L., Aird, J., et al. 2019, ApJ, 886, 11, doi: 10.3847/1538-4357/ab4a7c

Martín-Navarro, I., Brodie, J. P., Romanowsky, A. J., Ruiz-Lara, T., & van de Ven, G. 2018, Nature, 553, 307, doi: 10.1038/nature24999

Meena, B., Crenshaw, D. M., Schmitt, H. R., et al. 2021, ApJ, 916, 31, doi: 10.3847/1538-4357/ac0246

Molyneux, S. J., Rivera, G. C., Breuck, C. D., et al. 2023, The Quasar Feedback Survey: characterising CO excitation in quasar host galaxies. https://arxiv.org/abs/2310.10235

Morganti, R. 2017, Frontiers in Astronomy and Space Sciences, 4, 42, doi: 10.3389/fspas.2017.00042

Mullaney, J. R., Alexander, D. M., Fine, S., et al. 2013, Monthly Notices of the Royal Astronomical Society, 433, 622–638, doi: 10.1093/mnras/stt751

Murray, N., Quataert, E., & Thompson, T. A. 2005, The Astrophysical Journal, 618, 569–585, doi: 10.1086/426067

Newville, M., Stensitzki, T., Allen, D. B., & Ingargiola, A. 2015, LMFIT: Non-Linear Least-Square Minimization and Curve-Fitting for Python, 0.8.0, Zenodo, doi: 10.5281/zenodo.11813

Osterbrock, D. E., & Ferland, G. J. 2006, Astrophysics of gaseous nebulae and active galactic nuclei

Pfeifle, R. W., Weaver, K., Satyapal, S., et al. 2023, NuSTAR Observations of Four Mid-IR Selected Dual AGN Candidates in Galaxy Mergers. https://arxiv.org/abs/2306.16437

Pierce, J. C. S., Tadhunter, C., Ramos Almeida, C., et al. 2023, Monthly Notices of the Royal Astronomical Society, 522, 1736–1751, doi: 10.1093/mnras/stad455

Polednikova, J., Ederoclite, A., Cepa, J., et al. 2015, AA, 578, A121, doi: 10.1051/0004-6361/201525952

Ramos Almeida, C., Bischetti, M., García-Burillo, S., et al. 2022, Astronomy amp; Astrophysics, 658, A155, doi: 10.1051/0004-6361/202141906

Reyes, R., Zakamska, N. L., Strauss, M. A., et al. 2008, The Astronomical Journal, 136, 2373–2390, doi: 10.1088/0004-6256/136/6/2373

Salim, S., Rich, R. M., Charlot, S., et al. 2007, The Astrophysical Journal Supplement Series, 173, 267–292, doi: 10.1086/519218

Schlafly, E. F., & Finkbeiner, D. P. 2011, ApJ, 737, 103, doi: 10.1088/0004-637X/737/2/103

Singha, M., O'Dea, C. P., & Baum, S. A. 2023, Galaxies, 11, doi: 10.3390/galaxies11040085

Soderblom, D., et al. 2022, COS Data Handbook, 5th edn., Space Telescope Science Institute, Baltimore

Somalwar, J., Johnson, S. D., Stern, J., et al. 2020, ApJL, 890, L28, doi: 10.3847/2041-8213/ab733d

Stern, J., Behar, E., Laor, A., Baskin, A., & Holczer, T. 2014, Monthly Notices of the Royal Astronomical Society, 445, 3011–3024, doi: 10.1093/mnras/stu1960

Stern, J., Faucher-Giguère, C.-A., Zakamska, N. L., & Hennawi, J. F. 2016, The Astrophysical Journal, 819, 130, doi: 10.3847/0004-637x/819/2/130

Su, K.-Y., Hopkins, P. F., Bryan, G. L., et al. 2021, Monthly Notices of the Royal Astronomical Society, 507, 175, doi: 10.1093/mnras/stab2021

Sun, A.-L., Greene, J. E., & Zakamska, N. L. 2017, ApJ, 835, 222, doi: 10.3847/1538-4357/835/2/222

Tremonti, C. A., Heckman, T. M., Kauffmann, G., et al. 2004, ApJ, 613, 898, doi: 10.1086/423264

Weigel, A. K., Schawinski, K., Caplar, N., et al. 2017, ApJ, 845, 134, doi: 10.3847/1538-4357/aa803b

York, D. G., Adelman, J., Anderson, John E., J., et al. 2000, AJ, 120, 1579, doi: 10.1086/301513

Zakamska, N. L., & Greene, J. E. 2014, MNRAS, 442, 784, doi: 10.1093/mnras/stu842